doi: 10.34248/bsengineering.1723258



## **Research Article**

Volume 8 - Issue 5: 1504-1513 / September 2025

# THE EFFECT OF COMMON-MODE NOISE IN QUADRATURE RADAR SYSTEMS: ROTATING DISC IMBALANCE ESTIMATION

Yunus Emre ACAR1\*

<sup>1</sup>Selcuk University, Faculty of Technology, Department of Electrical and Electronics Engineering, 42075, Konya, Türkiye

Abstract: Accurate and robust detection of imbalance in rotating machinery is critical for ensuring operational reliability in industrial environments. This study experimentally investigates the impact of common-mode noise (CN) on feature-based classification performance in quadrature radar systems, estimating the imbalance level in a rotating disk. The proposed methodology utilizes a homodyne radar architecture to acquire in-phase (I) and quadrature (Q) baseband signals, from which time-domain features are extracted. A Hilbert transform-based denoising approach is implemented to address the detrimental effects of CN caused by electromagnetic interference and hardware imperfections. The extracted features, both from raw and denoised signals, are evaluated using various machine learning classifiers, including Decision Trees, Support Vector Machines, k-nearest Neighbors, Artificial Neural Networks, and ensemble methods. Experimental results demonstrate that CN significantly degrades classification accuracy, particularly for features derived from the amplitude and phase of complex-valued signals. The application of the proposed denoising technique yields a substantial improvement in classification metrics, with k-nearest Neighbors and Support Vector Machines achieving over 97% accuracy on the denoised data. The findings highlight the importance of effective noise mitigation in radar-based condition monitoring pipelines and establish the practical viability of quadrature radar systems for non-contact, high-precision imbalance detection in rotating machinery.

Keywords: Classification, Fault diagnosis, Feature extraction, Noise removal, Radar, Vibration

\*Corresponding author: Selcuk University, Faculty of Technology, Department of Electrical and Electronics Engineering, 42075, Konya, Türkiye E mail: yacar@selcuk.edu.tr (Y.E. ACAR)

Yunus Emre ACAR https://orcid.org/0000-0002-6809-9006

Received: June 19, 2025 Accepted: August 16, 2025 Published: September 15, 2025

 $\textbf{Cite as:} \ \textit{Acar YE. 2025}. \ \textit{The effect of common-mode noise in quadrature radar systems:} \ \textit{rotating disc imbalance estimation.} \ \textit{BSJ Eng Sci, 8(5): 1504-1513}.$ 

## 1. Introduction

Fault diagnosis and monitoring of rotating machinery are crucial for maintaining production efficiency and extending equipment lifespan within industrial settings (Li et al., 2023; Zhao et al., 2025). The imbalance, among the prevalent faults, is a significant concern, potentially leading to detrimental outcomes such as bearing damage, excessive vibration, energy wastage, and catastrophic machinery failures if not identified promptly (Cho et al., 2018). This issue substantially contributes to increased maintenance expenditures and unforeseen operational downtimes in rotating machinery.

While traditionally identified through contact-based vibration sensors, this approach faces several practical limitations, including susceptibility to sensor wear and degradation, challenges in sensor installation and maintenance in confined or inaccessible locations, signal interference from mechanical couplings, and reduced reliability in environments characterized by high temperatures, excessive contamination, or hazardous conditions. Consequently, operating non-contact measurement techniques have garnered considerable attention promptly (Goyal et al., 2020; Liu et al., 2025; Xu et al., 2025). In this regard, radar systems present a compelling alternative for industrial applications, owing to their inherent capabilities in target detection, tracking, and identification (Hansen et al., 2022; Acar, 2024).

Radar-based non-contact measurement methodologies promise reliable imbalance detection, even within demanding industrial environments. Contemporary radar systems frequently employ signals derived from quadrature demodulation for classification tasks. The cooperative use of in-phase (I) and quadrature (Q) signals, which exhibit a 90-degree phase difference, ensures the preservation of both amplitude and phase information integral to their complex-valued representation. This complex signal structure offers a rich dataset for applications such as discerning varying levels of imbalance in rotating machinery.

Nevertheless, common-mode noise (CN) presents a substantial challenge in such radar systems (Du et al., 2022). CN concurrently affects both I and Q signals acquired through IQ demodulation, degrading overall system performance. Key sources of this noise, particularly prevalent in industrial contexts, include electromagnetic interference, power supply fluctuations, and hardware imperfections. The presence of CN can introduce distortions in complex-valued signal parameters, complicating the accurate classification of different imbalance severities.

BSJ Eng Sci / Yunus Emre ACAR



Although the existing literature describes various noise mitigation techniques (Ge et al., 2025; Park et al., 2025), there is a lack of studies on the specific impact of CN on imbalance detection within industrial radar applications. This study systematically handles the effect of CN in quadrature radar signals on the performance of classifiers using features derived from complex-valued radar data and evaluates the impact of CN reduction. Although various noise reduction methods are available in the literature, the study examines a practical Hilbert transform-based CN elimination approach. It contributes by demonstrating the negative effect of CN on classification accuracy and determining to what extent the selected methods successfully reduce this impact, especially in the complex feature framework. This analysis highlights the importance of CN removal in radar processing chains.

Our methodological approach begins with experimentally acquired radar signals known to contain CN. We then subject these signals to a CN denoising process. Following the noise reduction step, we extract discriminative features from the complex-valued I+jQ signals, for both the original noisy signals (as a baseline) and the processed, denoised signals. These features are chosen based on their effectiveness in classification literature (Nayana and Geethanjali, 2017). In the final stage, these feature sets become the input for training and rigorously testing standard machine learning classifiers, such as Decision Tree (DT), Support Vector Machine (SVM),  $K^{th}$  Nearest Neighbors (KNN), Artificial Neural Network

(ANN), and some ensemble ones. The core of our analysis involves quantitatively evaluating and comparing the resulting classification performance and assessing the impact of each denoising technique.

The rest of the study is structured as follows. Section 2 provides detailed information on the experimental setup, dataset, mathematical background, feature extraction, classification, and evaluation criteria. Section 3 presents the experimental findings and a comprehensive assessment. Finally, the last section concludes the study.

## 2. Materials and Methods

#### 2.1. The experimental Setup

This section details the experimental apparatus used for this investigation. A versatile test rig designed by PiriTech was employed. This setup enables the simulation of common industrial faults such as winding defects, bearing failures, rotor bar damage, shaft misalignment (horizontal and vertical), and mechanical imbalance. Our research utilizes this platform to focus on imbalance faults intentionally introduced at different severity levels.

A 1.1 kV three-phase asynchronous motor rotated a metal disc at different speeds and loads. Imbalance levels were systematically created by attaching weights to threaded mounting points on the disc: 0 g (normal), 10 g (slight imbalance), 20 g (moderate imbalance), and 30 g (severe imbalance). Figure 1 illustrates the experimental configuration, and Table 1 lists the key components.

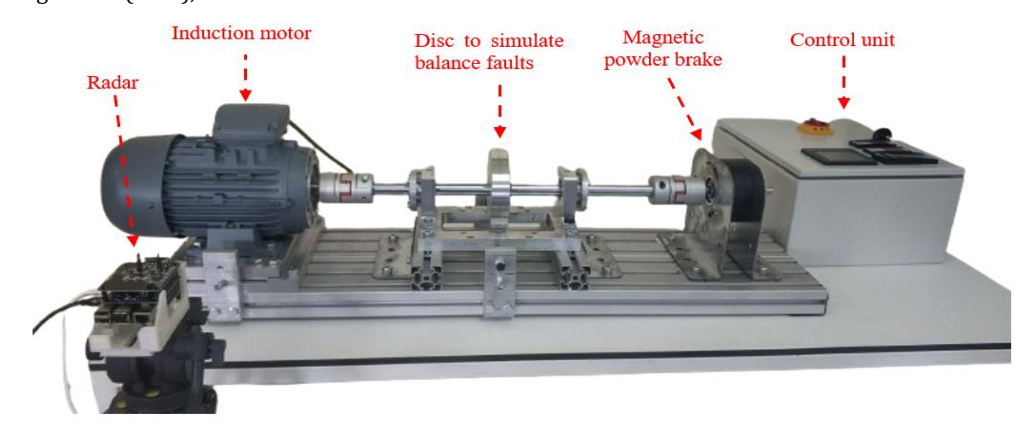


Figure 1. The experimental setup.

**Table 1.** Key components of the experimental test rig

Component	Specifications	Explanation
Volt VM 90S-4	1.1 kW, 1500	the monitored
Induction motor	rpm, 3-phase	motor
ABB ACS150- 01E-07A5-2 motor driver	50/60 Hz, 220V, 1.5 kW	controls the motor speed
EMF ABTF02 mag. powd. brake	15 Nm, 24 W, 24 V <sub>in</sub>	load for the motor
EMF TFD-02 mag. powd. brake driver	12-48 VDC, operation options (4-20 mA, 0-10V)	drives the load

A radar system based on the RFBEAM KLC5 transceiver module was employed. The module features a Homodyne receiver architecture, which directly provides baseband I and Q signals. Following the manufacturer's recommended circuit design, I/Q signal outputs were amplified by approximately 40 dB. Subsequently, the amplified signals were digitized using a Measurement Computing MCC118 Data Acquisition (DAQ) card. The Raspberry Pi 4 managed the data logging process, saving the acquired digital data into a CSV file format. Figure 2 illustrates this compact, Raspberry Pi-based data acquisition setup.

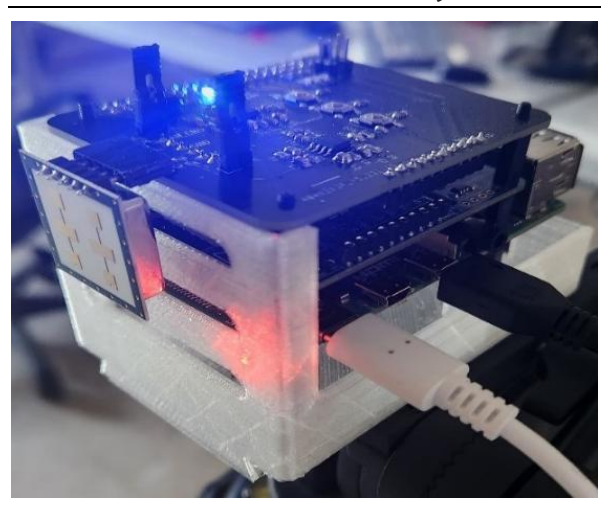


Figure 2. The radar hardware for data acquisition.

#### 2.2. The Dataset

For this four-class classification problem, encompassing the normal operating condition and three distinct levels of imbalance fault, a total of 1802 experimental trials were conducted. Each trial resulted in a 30-second data recording. The radar module, directed towards the motor from a distance of 30 cm, sampled the I/Q signals at a rate of 10 kSPS. The raw acquired data and a version processed to remove CN have been made publicly accessible to the research community via the KAGGLE platform (Acar,2025). Table 2 provides a detailed breakdown of the amount of data recordings obtained for each of the four classes.

Table 2. Class distribution in the dataset

Class Name	# of data
normal	462
slight imbalance	464
moderate imbalance	413
severe imbalance	463

In constructing the dataset for each classification category, we systematically varied the operational parameters of the motor. The rotational speed was incrementally adjusted across a comprehensive range from 500 to 1500 rpm, with precise 100 rpm intervals between test conditions. We implemented a methodical variation in mechanical loading conditions for each speed level. The load modulation was precisely controlled via a magnetic powder brake mechanism, varying from minimal loading (0%) to quarter-capacity loading (25% of the maximum 15 Nm torque capacity). We conducted repeated measurement sessions at different intervals to enhance statistical robustness and monitor temporal variations in system response.

#### 2.3. IQ Demodulation

Homodyne, or Direct-Conversion (Zero-IF), receiver architectures offer significant advantages in radar system design primarily because they simplify the overall structure. By eliminating the need for an Intermediate Frequency (IF) stage, these architectures reduce

component count, lower power consumption, decrease cost, and readily support monolithic integration onto a single chip. These factors make homodyne designs attractive for cost-sensitive, low-power, or highly integrated radar applications, such as automotive sensors or short-range presence detection.

Within this simplified framework, quadrature (IQ) demodulation, performed directly at the baseband, provides a key technique for extracting crucial target information, particularly velocity direction. Modern radar systems employing these homodyne architectures utilize IQ demodulation to directly convert the received Radio Frequency (RF) echo signal into its baseband I and Q components. The demodulation process maintains these components in phase quadrature (a 90-degree phase separation).

In this architecture, the Local Oscillator (LO) signal operates at the same frequency ( $f_c$ ) as the transmitted carrier signal. The system derives this LO signal directly from the transmitter's frequency source for phase coherence. A power splitter then divides the LO signal to generate the two reference signals in phase quadrature as in equation 1 and equation 2.

$$I_{ref} = \cos 2\pi f_c t \tag{1}$$

$$Q_{ref} = \sin 2\pi f_c t \tag{2}$$

The antenna captures the RF echo signal reflected from the vibrating target. This received signal,  $S_r(t)$ , carries the phase modulation imparted by the target's time-varying displacement x(t). Its phase relative to the transmitted signal can be expressed as equation 3

$$\phi(t) = \phi_0 + \frac{4\pi x(t)}{\lambda} \tag{3}$$

where  $\lambda$  is the carrier wavelength  $(c/f_c)$  and  $\phi_0$  represents the static phase shift due to the average target distance and system delays. The received signal is thus (equation 4):

$$S_r(t) \approx A_R cos(2\pi f ct + \phi_0 + \frac{4\pi x(t)}{\lambda})$$
 (4)

where  $A_R$  is the received signal amplitude.

The receiver front-end directly mixes this incoming RF signal  $S_r(t)$  independently with both the I and Q reference signals. Two parallel low-pass filters then reject the high-frequency mixing, yielding the baseband I and Q signals (equation 5.1 and 5.2):

$$I(t) = K \cos(\phi_0 + \frac{4\pi x(t)}{\lambda})$$
 (5.1)

$$Q(t) = K \sin(\phi_0 + \frac{4\pi x(t)}{\lambda})$$
 (5.2)

Here, K represents the overall gain and amplitude factors. These I/Q signals encode the target's vibration information within their relative phase. By treating the outputs as a complex baseband signal C(t) = I(t) + jQ(t),

one can robustly extract the instantaneous phase angle (equation 6):

$$arctan2(Q(t),I(t)) = \phi_0 + \frac{4\pi x(t)}{\lambda}$$
 (6)

The arctan2 function resolves phase ambiguities across the 360-degree range. Subsequent processing involves unwrapping this phase angle (if necessary) and removing the static phase offset  $\phi_0$  (often achieved through highpass filtering or baseline subtraction). Finally, we recover the target's vibration displacement waveform x(t) by scaling the dynamic phase component (equation 7):

$$x(t) = \frac{\lambda}{4\pi} \times (arctan2(C(t)) - \phi_0)$$
 (7)

This homodyne IQ demodulation scheme allows direct conversion of the target's micro-scale motion x(t) into measurable baseband phase variations, forming the basis for our vibration analysis. Figure 3 illustrates the described receiver architecture.

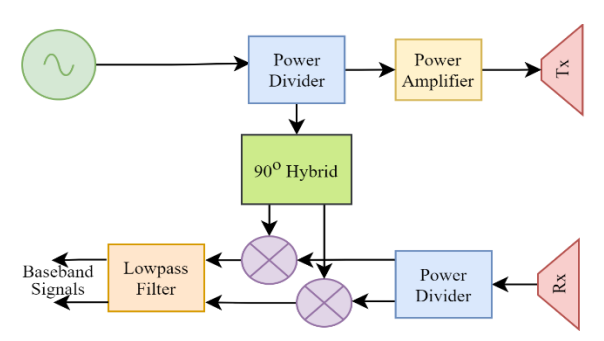


Figure 3. Block scheme of an IQ demodulated CW radar.

## 2.4. CN Removal

CN can be expressed for IQ demodulated receivers as noise that affects both quadrature signals equally, as shown in equations 8.a and 8.b.

$$I_n(t) = K \cos \left( \phi_0 + \frac{4\pi x(t)}{\lambda} \right) + noise \tag{8.a}$$

$$Q_n(t) = K \sin\left(\phi_0 + \frac{4\pi x(t)}{\lambda}\right) + noise \tag{8.b}$$

System performance can be considerably compromised by CN in hardware configurations where dedicated CN elimination mechanisms are absent or in architectures with simplified complexity.

This research employs a methodology centered on Hilbert transformation techniques to extract CN-removed I and Q signals. The Hilbert transform represents a mathematical operation that generates a phase-quadrature version of the original signal, shifted by precisely 90 degrees. In formal mathematical terms, when applied to a signal f(t), the Hilbert transform  $H\{f(t)\}$  is characterized as the convolution integral of the signal with the function  $1/(\pi t)$ . In this approach, the difference between the noisy signals, D(t), is initially obtained as expressed in equation 9.

$$D(t) = I_n(t) - Q_n(t)$$

$$= K[cos(\phi(t)) - sin(\phi(t))]$$
(9)

When the Hilbert transform is applied to this difference signal, the  $D_q(t)$  signal is obtained as presented in equation 10.

$$D_q(t) = H\{D(t)\}$$

$$= K[\sin(\phi(t)) + \cos(\phi(t))]$$
(10)

The noise-free baseband signals I(t) and Q(t) are recovered through the combined utilization of these signals as formulated in equation 11 and equation 12.

$$I(t) = \frac{D(t) + D_q(t)}{2} = K\cos(\phi(t))$$
(11)

$$Q(t) = \frac{D_q(t) - D(t)}{2} = Ksin(\phi(t))$$
(12)

#### 2.5. Feature Extraction

Feature extraction is a critical stage in machine learning-based classification applications. Numerous studies have demonstrated effective feature extraction methods in both time and frequency domains for applications like vibration-based machine health monitoring and fault diagnosis (Zhao et al., 2023; Jiao et al., 2025). While frequency domain features obtained through time-frequency transformations often improve classification performance (Kilic and Acar, 2024), time domain feature extraction offers simplicity and superior capability in capturing transient events. Direct usage of time domain signals reduces complexity across many applications (Wang et al., 2022).

This study focuses on time domain features with proven classification efficacy from windowed signals. We constructed the complex signal  $\mathcal{C}(t)$  from 30-second recordings and divided its amplitude and phase components into 1-second windows with 50% overlap. For each signals, we calculated 12 features by averaging the values extracted from individual windows. We applied this extraction methodology to raw signals and those processed with the CN reduction approach. Equations 13-24 present the mathematical formulations of these extracted features.

Mean Absolute Value (MAV): Equation 13 demonstrates the calculation method for this particular feature, which represents the arithmetic average of absolute sample magnitudes within the analyzed segment.

$$MAV = \frac{1}{L} \sum_{n=1}^{L} |x[n]| \tag{13}$$

Energy (E): The segment's power content is quantified by this feature, with its mathematical computation presented in equation 14.

$$E = \sum_{n=1}^{L} x[n]^2 \tag{14}$$

Waveform Length (WL): This feature corresponds to the sum of absolute differences between consecutive samples. It represents the sum of absolute first-order derivatives,

providing information about the signal's roughness, rate of change, and frequency characteristics for discrete signals. WL is calculated as shown in equation 15.

$$WL = \sum_{n=1}^{L} |x[n] - x[n-1]|$$
 (15)

Willison Amplitude (WA): This metric evaluates sequential sample variations against a predetermined threshold, tallying occurrences where the differential surpasses this boundary value. The quantification process utilizes the mathematical framework outlined in equations 16.a and 16.b.

$$WA = \sum_{n=1}^{L} f|x[n] - x[n+1]|$$
 (16.a)

$$f(x) = \begin{cases} 1 & \text{if } x \ge \varepsilon \\ 0 & \text{otherwise} \end{cases}$$
 (16.b)

Zero Crossing (ZC): This parameter quantifies the frequency of axis intersections throughout the segment. The mathematical formulation in equation 17.a identifies an axis crossing when adjacent values exhibit sign reversal. An additional verification can eliminate insignificant fluctuations near the zero line and confirm that the magnitude difference between consecutive samples exceeds a defined threshold, as formulated in equation 17.b.

$$ZC = \sum_{n=1}^{L} (x[n] \times x[n+1]) < 0$$
 (17.a)

$$(|x[n] - x[n+1]|) > \varepsilon \tag{17.b}$$

Slope Sign Change (SSC): This metric counts directional reversals in the signal trajectory throughout the segment. Equation 18 provides the mathematical framework for identifying these gradient sign changes. Only instances where consecutive sample differences exceed a defined threshold are counted, following the criterion specified in equation 17.b.

$$SSC = \sum_{n=1}^{L} ((x[n+1] - x[n]) \times (x[n] - x[n-1])) < 0$$
 (18)

Root Mean Square (RMS): Equation 19 presents the mathematical formulation for this feature, which computes the square root of the average of squared values across the segment.

$$RMS = \sqrt{\frac{1}{L} \sum_{n=1}^{L} x[n]^2}$$
 (19)

Mean  $(\mu)$ : This parameter determines the arithmetic average across all points within the segment, computed according to the formula presented in equation 20.

$$Mean = \mu = \frac{1}{L} \sum_{n=1}^{L} x[n]$$
 (20)

Variance ( $\sigma^2$ ): This metric evaluates the dispersion of values by measuring squared deviations from the central tendency. The mathematical average of these squared differentials yields the variance parameter. Equation 21 presents the computational framework for determining this statistical dispersion value for each analyzed segment.

Variance = 
$$\sigma^2 = \frac{1}{L} \sum_{n=1}^{L} (x[n] - \mu)^2$$
 (21)

Standard Deviation (STD): This parameter quantifies the degree of dispersion by extracting the square root of the variance value, as mathematically formulated in equation 22.

$$STD = \sigma = \sqrt{\frac{1}{L} \sum_{n=1}^{L} (x[n] - \mu)^2}$$
 (22)

Skewness (SKW): This attribute quantifies distributional asymmetry characteristics. For perfectly symmetric distributions, it yields a zero value. In asymmetric cases, the parameter's sign indicates directional bias—positive values denote rightward skewing while negative values indicate leftward skewing. Equation 23 provides the mathematical framework for calculating this distributional asymmetry metric for each segment.

$$SKW = \frac{\frac{1}{L}\sum_{n=1}^{L}(x[n] - \mu)^{3}}{\sigma^{3}}$$
 (23)

Kurtosis (KURT): This parameter evaluates the peakedness or flatness characteristics of a distribution profile. As formulated in equation 24, the KURT value for each segment offers a numerical assessment of the distribution's morphology compared to the Gaussian curve.

$$KURT = \frac{\frac{1}{L}\sum_{n=1}^{L}(x[n] - \mu)^4}{\sigma^4}$$
 (24)

Feature extraction procedures were applied separately to amplitude and phase signals, and by combining the extracted features, a total of 24 features were generated for each data sample to be input into the classifier.

#### 2.6. Classification

The four-class imbalance detection problem was addressed by well-known machine learning approaches with the dataset comprising 1802 experiments. The performance of these methods was validated using 5-fold cross-validation. The hyperparameters of the classifiers were optimized through a systematic grid search methodology. This process involved evaluating all possible hyperparameter combinations within predefined ranges at specific incremental steps. Performance metrics were assessed for each parameter configuration, enabling the identification of the optimal hyperparameter set that maximizes the model's generalization capability. Table 3 summarizes the parameter searching ranges for the preferred classifiers.

#### 2.7. Performance Metrics

The effectiveness of the classifiers is evaluated through confusion matrices. These matrices are tabular representations that show how the model's predictions align with each class, functioning as an assessment tool for model performance. Figure 4 illustrates a multi-class confusion matrix.

**Table 3.** Hyperparameter searching ranges for the classifiers

Method	Parameters
	Kernel function: linear, quadratic, cubic
SVM	box constraint level: 0.001-1.0
	multiclass meth.: one vs one, one vs all
	number of neighbors: 1-901
	distance metric: Euclidean, Chebyshev,
KNN	cosine, Hamming, cubic.
	distance weight: equal, inverse, squared
	inverse.
	Max. # of splits: 1-1801
DT	split criterion: Gini diversity index,
וע	twoing rule, maximum deviance
	reduction.
	Ensemble method: Bag, AdaBoost,
	RUSBoost.
Ensemble	# of learners:10-50
	learning rate:0.001-1.0
	max. # of splits: 1-1801
ANN	# of fully connected layer: 1-3
	activation func.: sigmoid, tanh, ReLU,
	none.
	$lambda: 5 \times 10^{-9} - 50$
	first layer size:1-300
	second layer size:1-300
	third layer size:1-300

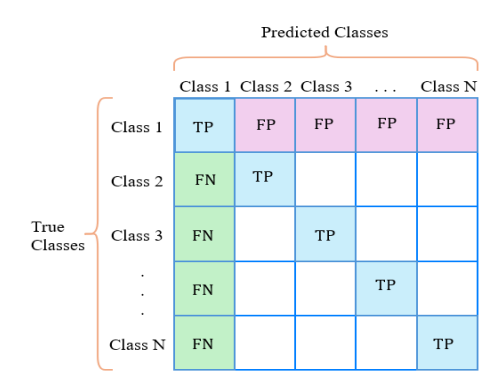


Figure 4. A multi-class confusion matrix.

The confusion matrix's True Positive (TP), False Positive (FP), and False Negative (FN) values are used to compute various assessment metrics. equations 25 through 28

present the metrics and formulas employed.

$$Accuracy = (\Sigma TPs) / (All predictions)$$
 (25)

$$Precision = TP / (TP + FP)$$
 (26)

$$Recall = TP / (TP + FN)$$
 (27)

F1 score = 
$$2 \times (Precision \times Recall) / (Precision + Recall)$$
 (28)

Within formulas (25)-(28), TP values indicate successful classification for individual classes. Accuracy represents the proportion of total TP values, showing how well the model correctly classifies the issue. Precision reflects the accuracy of the positive predictions, emphasizing its capability to reduce FP values. The Recall metric, meanwhile, gauges how effectively the model identifies actual positives, showcasing its ability to minimize FN values

In the context of the four-class imbalance detection problem, precision and recall metrics have been calculated discretely for each class. This calculation methodology yields four distinct precision and recall values corresponding to the four classes. For the final metric values in the analysis, we have implemented an averaging approach of the class-wise precision and recall metrics. The F1 score, the harmonic means of the average precision and recall metrics, has been utilized to evaluate the equilibrium between these metrics through collective assessment.

#### 3. Results and Discussion

This section presents the classification results obtained using different input configurations. The performance of the classifiers is reported both without and with CN removal. Table 4 summarizes the classification results obtained by directly using the radar baseband signals without applying CN removal. In Table 4, the feature set  $F_I$  refers to the 12 features extracted solely from the I signal,  $F_0$  denotes the features extracted exclusively from the Q signal,  $F_{abs}$  represents the features derived from the amplitude of the complex-valued signal formed by the Iand Q components, and  $F_{anale}$  corresponds to the features extracted from the phase of the complex-valued signal. The [ · ] operator indicates that the respective feature sets are used in combination. Each classifier was trained and evaluated separately with these different input sets, and the classification performance is reported in terms of accuracy, precision, recall, and F1 score. The complexity analysis of the models is conducted based on model size and prediction speed.

Table 4. The classification results without CN removal

	Input signal	Accuracy	Precision	Recall	F1	Prediction	Model Size
Model Name		(%)	(%)	(%)	Score	Speed (obs/s)	(kb)
					(%)		
				88.58			36
	$F_Q$	82.74	82.52	82.49	82.5	21000	48
DT	$[F_I F_Q]$	88.9	88.89	88.8	88.84	36000	35
<i>)</i> 1	$F_{abs}$	81.63	81.68	81.59	81.63	Speed (obs/s)           (%)           18.58         16000           18.58         16000           18.84         36000           18.84         36000           18.82         52000           18.21         13000           18.35         20000           18.35         20000           18.4         33000           18.68         45000           19.51         43000           19.51         4000           19.51         4000           19.49         15000           19.49         15000           19.40         88000           19.41         15000           19.40         88000           19.41         15000           19.42         4000           19.43         47000           19.44         88000           19.45         47000           19.48         730           19.48         730           19.48         730           19.46         420           19.48         13000	46
	$F_{angle}$	$ \begin{array}{c ccccccccccccccccccccccccccccccccccc$	49				
	$[F_{abs} F_{angle}]$	87.85	87.82	87.82	87.82	52000	39
	$F_I$	93.23	93.38	93.12	93.21	13000	387
	$F_Q$	93.4	93.4	93.34	93.35	20000	124
SVM	$[F_I F_Q]$	95.56	95.52	95.54	95.52	15000	155
O V IVI	$F_{abs}$	93.4	93.45	93.37	93.4	33000	225
	$F_{angle}$	88.79	88.68	88.68	88.68	45000	131
	$[F_{abs} F_{angle}]$	95.12	95.12	95.14	95.1	43000	156
	$F_I$	91.51	91.67	91.46	91.53	19000	216
	$F_Q$	91.24	91.22	91.16	91.16	14000	216
KNN	$[F_I F_Q]$	91.51	91.59	91.48	91.51	4000	395
XIVIV	$F_{abs}$	91.45	91.54	91.5	91.49	16000 21000 36000 54000 48000 52000 13000 20000 15000 33000 45000 43000 19000 14000 4000 15000 88000 67000 38000 44000 52000 47000 730 620 400 23000 13000	216
	$F_{angle}$	90.23	90.28	90.28	90.25	5000	218
	$[F_{abs} F_{angle}]$	94.12	94.13	94.16	94.12	15000	386
	$F_{I}$	94.40	94.47	94.36		88000	18
	$F_Q$	92.79	92.73	92.77	92.75	67000	169
NN	$[F_I F_Q]$	96.89	96.89	96.9	96.9	38000	32
NIN	$F_{abs}$	91.62	91.63	91.59	91.6	44000	37
	$F_{angle}$	91.95	91.91	91.89	91.89	52000	110
	$[F_{abs} F_{angle}]$	96.84	96.79	96.86	96.81	47000	74
	$F_{I}$	94.89	94.89	94.85	94.86	730	23000
	$F_Q$	89.62	89.54	89.43	89.46	620	32000
? l. l .	$[F_I F_Q]$	96.45	96.43	96.45	96.44	400	20000
Ensemble	$F_{abs}$	86.51	86.56	86.54	86.54	23000	824
		89.96	89.9	89.92	89.88	13000	2200
	$[F_{abs} F_{angle}]$	96.12	96.09	96.16	96.12	1700	7000

When examining the classification results obtained from non-denoised data, the NN model with the  $[F_I F_O]$ combination demonstrates superior performance, achieving an accuracy rate of 96.89%. This model also excels in other classification metrics, showing balanced precision (96.89%), recall (96.9%), and F1 score (96.9%), indicating its robust performance across all evaluation criteria. The NN model using the [abs angle] combination follows closely with 96.84% accuracy, 96.79% precision, 96.86% recall, and 96.81% F1 score, demonstrating consistent performance across metrics. From a model complexity perspective, NN models stand out not only for their high accuracy but also for their remarkably compact model sizes (18-169 kb) and rapid prediction speeds (38,000-88,000 observations per second). In contrast, Ensemble models, while achieving comparable accuracy levels (96.45%) and balanced precision (96.43%), recall (96.45%), and F1 score (96.44%), require substantially larger model sizes (7,000-32,000 kb) and operate at significantly slower prediction speeds (400-1,700 observations per second). SVM models demonstrate good

performance with moderate model sizes (124-387 kb) and prediction speeds (13,000-45,000 observations per second), maintaining consistent precision, recall, and F1 scores that closely track their accuracy values. Despite being the smallest and fastest, the decision tree model yields the lowest accuracy rates and corresponding classification metrics. These findings highlight the critical importance of model selection and signal feature combination strategies in quadrature signal classification. Notably, NN models emerge as the most suitable option for real-time applications by offering an optimal balance between computational efficiency and comprehensive classification performance across all evaluation metrics. Examining the classification results after CN removal reveals significant performance improvements across models as tabulated in Table 5. The KNN model with the  $[F_{abs\_c} F_{angle\_c}]$  combination achieves the highest accuracy at 97.45%, with corresponding precision (97.43%), recall (97.42%), and F1 score (97.41%) values demonstrating exceptional balance across metrics.

**Table 5.** The classification results with CN removal

Model Name	Input signal	Accuracy	Precision	Recall	F1	Prediction	Model Size
		(%)	(%)	(%)	Score	Speed (obs/s)	(kb)
					(%)		
	$F_{I\_c}$	83.24	83.08	83.09	83.07	64000	52
	$F_{Q\_c}$	83.24	83.15	83.11	83.13	6600	50
nт	$[F_{I\_c} \ F_{Q\_c}]$	85.96	85.89	85.9	85.89	37000	43
OT SVM KNN	$F_{abs\_c}$	85.18	85.17	85.12	85.13	56000	45
	$F_{angle\_c}$	81.47	81.4	81.42	81.38	56000	53
	$[F_{abs\_c} F_{angle\_c}]$	90.57	90.5	90.59	90.52	39000	38
	$F_{I\_C}$	92.79	92.64	92.7	92.66	20000	144
	$F_{Q\_c}$	92.73	92.63	92.63	92.61	25000	149
CYANA	$[F_{I\_c} F_{Q\_c}]$	93.9	93.82	93.85	93.82	42000	166
O V IVI	$F_{abs\_c}$	91.73	91.71	91.69	91.67	45000	98
	$F_{angle\_c}$	93.45	93.37	93.32	93.33	9900	237
	$[F_{abs\_c} F_{angle\_c}]$	97.29	97.26	97.28	97.26	30000	152
	$F_{I\_c}$	85.13	85.16	85.17	85.09	20000	216
	$F_{Q\_c}$	84.24	84.16	84.18	84.15	3500	218
ZNINI	$[F_{I\_c} F_{Q\_c}]$	86.9	86.85	86.9	86.86	9900	386
ZIVIV	$F_{abs\_c}$	92.79       92.64       92.7       92.66       20000         92.73       92.63       92.63       92.61       25000         93.9       93.82       93.85       93.82       42000         91.73       91.71       91.69       91.67       45000         93.45       93.37       93.32       93.33       9900         97.29       97.26       97.28       97.26       30000         85.13       85.16       85.17       85.09       20000         84.24       84.16       84.18       84.15       3500         86.9       86.85       86.9       86.86       9900         92.06       92.09       92.12       92.06       14000         92.45       92.38       92.36       92.37       8100         97.45       97.43       97.42       97.41       14000         93.51       93.41       93.46       93.4       57000         95.23       95.17       95.19       95.17       26000         95.89       95.87       95.89       95.87       74000         93.78       93.69       93.69       93.67       64000	216				
	$F_{angle\_c}$	92.45	92.38	92.36	92.37	8100	216
	$[F_{abs\_c} F_{angle\_c}]$	97.45	97.43	97.42	97.41	14000	386
	$F_{I\_C}$	93.51	93.41	93.46	93.4	57000	70
	$F_{Q\_c}$	94.4	94.32	94.27	94.28	65000	193
AINI	$[F_{I\_c} F_{Q\_c}]$	95.23	95.17	95.19	95.17	26000	284
NIN	$F_{abs\_c}$	95.89	95.87	95.89	95.87	74000	163
	$F_{angle\_c}$	93.78	93.69	93.69	93.67	64000	46
	$[F_{abs\_c} F_{angle\_c}]$	97.34	97.3	97.32	97.3	86000	19
	$F_{I\_c}$	91.73	91.65	91.65	91.64	7200	3000
	$F_{Q\_c}$	90.95	90.95	90.89	90.9	910	24000
Incomble	$[F_{I\_c} \ F_{Q\_c}]$	94.17	94.12	94.15	94.13	630	16000
Ensemble	$F_{abs\_c}$	92.01	92.05	92.0	92.02	810	25000
	$F_{angle\_c}$	88.57	88.45	88.46	88.46	850	21000
	$[F_{abs\_c} F_{angle\_c}]$	95.06	95.04	95.02	95.01	13000	891

This performance is closely followed by the SVM model using the same feature combination (97.29% accuracy) and the NN model (97.34% accuracy), showing similarly balanced precision, recall, and F1 scores.

The relationship between model complexity and performance also presents interesting patterns in the noise-removed scenario. Despite their previously modest performance, KNN models show improvement with noise removal, particularly with the  $[F_{abs\_c} \ F_{angle\_c}]$  combination, while maintaining moderate model sizes (386 kb) and reasonable prediction speeds (14,000 obs/s). NN models continue to offer an excellent balance of high accuracy and computational efficiency with small model sizes (19-284 kb) and impressive prediction speeds (26,000-86,000 obs/s). SVM models demonstrate substantial improvement with noise removal while maintaining moderate resource requirements.

The most striking transformation occurs in the

effectiveness of signal features. While  $[F_l F_Q]$  combinations dominated in the non-denoised scenario, the  $[F_{abs\_c} F_{angle\_c}]$  combination consistently outperforms all other feature combinations after noise removal across nearly all models. Additionally, individual  $F_{abs\_c}$  and  $F_{angle\_c}$  features show marked improvement compared to their non-denoised counterparts.

Comparing the Table 4 and Table 5 highlights the critical importance of CN noise removal in quadrature signal classification. The overall accuracy ceiling rises from 96.89% to 97.45%, but more importantly, the performance distribution across models and features changes significantly. The noise removal process enhances the discriminative power of amplitude and phase information, making the  $[F_{abs\_c} F_{angle\_c}]$  combination superior to the previously dominant  $[F_I F_Q]$  combination. This transformation suggests that CN disproportionately affects signal characteristics, and its removal allows previously obscured patterns to emerge.

Furthermore, the improved performance of simpler models like KNN after noise removal indicates that much of the classification challenge in the original data stemmed from noise rather than inherent signal complexity. These findings emphasize that implementing effective noise removal techniques can be as crucial as model selection in

achieving optimal classification performance, potentially allowing computationally lighter models without sacrificing accuracy in practical applications. The heatmap presented in Figure 5 visually summarizes the impact of CN removal on classification accuracy.

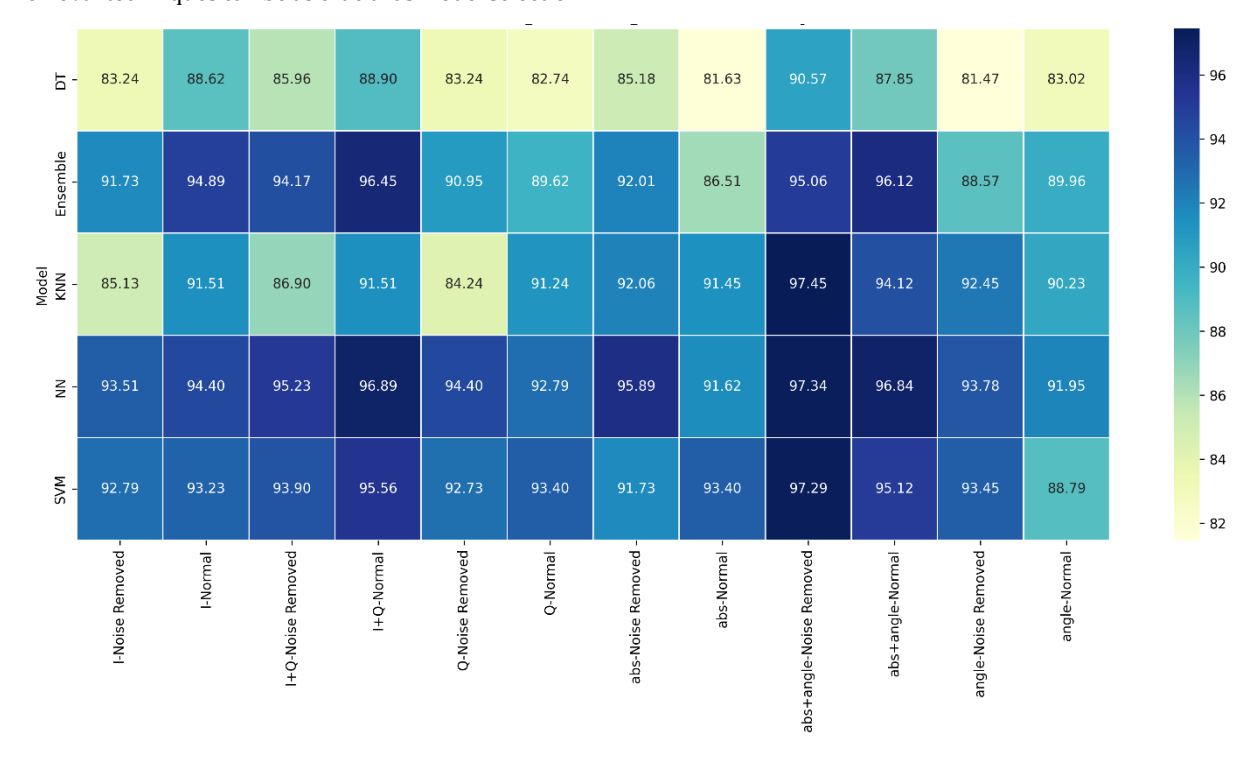


Figure 5. The impact of the CN-removal for each model and input type.

The heat map visualization presents a comprehensive comparative analysis of classification accuracy across multiple dimensions: machine learning models, signal feature combinations, and noise conditions. This multifactorial representation effectively illustrates the interaction between model selection and feature engineering in noisy and noise-removed scenarios.

The color gradient reveals a clear performance stratification, with the highest accuracy values (>97%) concentrated in the noise-removed  $[F_{abs\_c}\ F_{angle\_c}]$  combinations for KNN, SVM, and NN models. This pattern suggests a significant interaction between noise removal and the discriminative power of combined amplitude and phase information. The visualization demonstrates that while  $[F_I\ F_Q]$  combinations generally outperform other feature sets in normal conditions, the CN removal fundamentally alters this relationship, elevating  $[F_{abs\_c}\ F_{angle\_c}]$  combinations to superior performance.

The heat map also effectively captures the differential impact of noise removal across models. The dramatic improvement in KNN performance with noise-removed amplitude and phase features (from 94.12% to 97.45%) represents a particularly noteworthy transition, suggesting that this model's classification boundaries become substantially more effective when the CN is eliminated. Conversely, the relatively modest improvements in some DT model configurations indicate

potential limitations in the model's ability to leverage enhanced signal quality.

From a methodological perspective, this visualization provides valuable insights for optimizing classification pipelines in quadrature signal processing applications. It demonstrates that optimal model selection may differ significantly between noisy and clean signal conditions, challenging the assumption that more complex models necessarily yield better performance. The heat map also indicates that appropriate noise removal techniques potentially allow simpler, computationally efficient models to achieve performance comparable to or exceeding that of more complex alternatives in noisy environments.

#### 4. Conclusion

This study investigated the classification of quadrature radar signals using machine learning methods and the impact of CN removal on classification performance. The results demonstrate that radar-based systems offer an effective solution for detecting imbalance in rotating machinery.

The elimination of CN noise led to significant transformations in classification performance. The most striking improvement was observed in the KNN model with the  $[F_{abs\_c}\ F_{angle\_c}]$  combination, where accuracy increased from 94.12% to 97.45%. Furthermore, the noise

removal process fundamentally altered the effectiveness of signal features, elevating the [abs angle] combination to superiority over the  $[F_I F_O]$  combination.

The superiority of radar-based solutions lies in their ability to detect imbalance from a safe distance without requiring physical intervention with machinery. The capability of radar signals to detect movements with millimeter precision enables early-stage detection of imbalance.

Accuracy rates exceeding 97% confirm that radar-based systems represent a high-performance solution for imbalance detection. The combined use of noise-removed amplitude and phase information demonstrates the effectiveness of radar signals in capturing imbalance characteristics.

Unlike conventional vibration sensor-based approaches, radar systems enable simultaneous monitoring of multiple machines, offering a cost-effective monitoring solution for industrial facilities.

Future research will explore the capability of radar-based systems to detect imbalance location and provide automatic correction recommendations. This development transforms radar technology from a passive monitoring tool into an active troubleshooting solution.

#### **Author Contributions**

The percentages of the author' contributions are presented below. The author reviewed and approved the final version of the manuscript.

	Y.E.A.	
С	100	
D	100	
S	100	
DCP	100	
DAI	100	
L	100	
W	100	
CR	100	
SR	100	
PM	100	
FA	100	

C=Concept, D= design, S= supervision, DCP= data collection and/or processing, DAI= data analysis and/or interpretation, L= literature search, W= writing, CR= critical review, SR= submission and revision, PM= project management, FA= funding acquisition.

#### **Conflict of Interest**

The author declared that there is no conflict of interest.

#### **Ethical Consideration**

Ethics committee approval was not required for this study because of there was no study on animals or humans.

#### References

- Acar YE. 2024. Radar-enabled non-contact speed estimation for rotating electrical machinery. Meas, 235: 114989.
- Acar YE. 2025. Radar data for rotational mass imbalance detection. URL:
  - https://www.kaggle.com/datasets/yunusemreacar1/radar-data-for-machine-fault-detection (accessed date: August 11, 2025).
- Cho S, Gao Z, Moan T. 2018. Model-based fault detection, fault isolation and fault-tolerant control of a blade pitch system in floating wind turbines. Renew Energy, 120: 306-321.
- Du M, Zhong P, Cai X, Bi D. 2022. DNCNet: Deep radar signal denoising and recognition. IEEE Trans Aerosp Electron Syst, 58(4): 3549-3562.
- Ge Y, Wang R, Zeng X. 2025. Robust and accurate eye-blink detection using a 24-GHz CW radar. IEEE Trans Instrum Meas, 74: 1-10.
- Goyal D, Dhami SS, Pabla BS. 2020. Non-contact fault diagnosis of bearings in machine learning environment. IEEE Sens J, 20(9): 4816-4823.
- Hansen S, Bredendiek C, Briese G, Froehly A, Herschel R, Pohl N.
   2022. A SiGe-chip-based D-band FMCW-radar sensor with 53-GHz tuning range for high resolution measurements in industrial applications. IEEE Trans Microw Theory Tech, 70(1): 719-731
- Jiao H, Sun W, Wang H, Wan X. 2025. Comprehensive exploitation of time- and frequency-domain information for bearing fault diagnosis on imbalanced datasets via adaptive wavelet-like transform general adversarial network and ensemble learning. Sensors, 25(7): 2328.
- Kilic ME, Acar YE. 2024. Performance evaluation of the time-frequency transformation methods on electrical machinery fault detection. Bitlis Eren Univ J Sci, 13: 1147-1157.
- Li H, Wu X, Liu T, Li S. 2023. Rotating machinery fault diagnosis based on typical resonance demodulation methods: A review. IEEE Sens J, 23(7): 6439-6459.
- Liu H, Ji D, Lin J, Liu Z, Li H. 2025. Residual angular speed analysis based on laser Doppler vibrometer and its application in planetary gearbox diagnosis. Meas, 250: 116987.
- Nayana BR, Geethanjali P. 2017. Analysis of statistical time-domain features effectiveness in identification of bearing faults from vibration signal. IEEE Sens J, 17(17): 5618-5625.
- Park JE, Lee GH, Lee IS, Yang JR. 2025. Heart rate extraction technique with mitigation of respiration harmonic for bioradar sensors. IEEE Sens J, 25(1): 929-939.
- Wang H, Sun W, He L, Zhou J. 2022. Rolling bearing fault diagnosis using multi-sensor data fusion based on 1D-CNN model. Entropy, 24(5): 573.
- Xu W, He J, Li G, Wu C, Lv J, Qian C. 2025. Progressive orthogonal matching pursuit and adaptive modal screening for fault diagnosis of rotating machinery components using acoustic signals. Meas, 252: 117345.
- Zhao N, Zhang J, Mao Z, Jiang Z, Li H. 2023. Time-frequency feature extraction method of the multi-source shock signal based on improved VMD and bilateral adaptive Laplace wavelet. Chin J Mech Eng, 36(1): 36.
- Zhao Y, Yang X, Huang J, Gao J, Zhou X, Zhang T. 2025. Ensemble targeted stacked denoising autoencoders with mutual information constraint for rotating machinery fault diagnosis. IEEE Trans Ind Inform, 21(2): 1329-1338.